Electronic Supplementary Material (ESI) for Nanoscale.

Supplementary Information for:

Fast Capture and Multiplexed Detection of Short Multi-Arm DNA Stars in Solid-State Nanopores

Liqun He, Philipp Karau, Vincent Tabard-Cossa*

Department of Physics, University of Ottawa, Ottawa, ON, Canada

*corresponding author: tcossa@uOttawa.ca,

Table of Contents

Supplementary Section S1: Assembly and Sequences for Star-shaped Structures

Following Wang *et al.* [1] the sequences for the N-arm star nanostructures are:

4-arm star:

strand 1	5'	GTGTCTTGAAGAAGGACCAGGGAACGTATTTGCCTTGTCTGGGAAATCGT	3'
strand 2	5'	ACGATTTCCCAGACAAGGCAAATACGGACTTATCGTTTGCTAATACTACA	3'
strand 3	5'	TGTAGTATTAGCAAACGATAAGTCCCCAACTGGTTGTGGCCTATCGAAAA	3'
strand 4	5'	TTTTCGATAGGCCACAACCAGTTGGGTTCCCTGGTCCTTCTTCAAGACAC	3'

6-arm star:

strand 1	5'	AGGCACAGCTATAATAACGCAATCCTCTCCGGCCTCAAACTACTTTACCT	3'
strand 2	5'	AGGTAAAGTAGTTTGAGGCCGGAGACCGAATGGAGTCTGTTCTCGACGCT	3'
strand 3	5'	AGCGTCGAGAACAGACTCCATTCGGACAATTACGAACCAACTTAGGACCT	3'
strand 4	5'	AGGTCCTAAGTTGGTTCGTAATTGTGGTCATCGTGGCGTACCATATACCT	3'
strand 5	5'	AGGTATATGGTACGCCACGATGACCTCTTCGATCTACCCGATAGGCTCCT	3'
strand 6	5'	AGGAGCCTATCGGGTAGATCGAAGAGGATTGCGTTATTATAGCTGTGCCT	3'

8-arm star:

strand 1	5'	AGGCACAGCTATAATAACGCAATCCTCTCCGGCCTCAAACTACTTTACCT	3'
strand 2	5'	AGGTAAAGTAGTTTGAGGCCGGAGACCGAATGGAGTCTGTTCTCGACGCT	3'
strand 3	5'	AGCGTCGAGAACAGACTCCATTCGGACAATTACGAACCAACTTAGGACCT	3'
strand 4	5'	AGGTCCTAAGTTGGTTCGTAATTGTGGTCATCGTGGCGTACCATATACCT	3'
strand 5	5'	AGGTATATGGTACGCCACGATGACCTCTTCGATCTACCCGATAGGCTCCT	3'
strand 6	5'	AGGAGCCTATCGGGTAGATCGAAGACGTACAGGTGTGACTTGAATTTGCT	3'
strand 7	5'	AGCAAATTCAAGTCACACCTGTACGAGTGTTAGAATACAACAAGCGACCT	3'
strand 8	5'	AGGTCGCTTGTTGTATTCTAACACTGGATTGCGTTATTATAGCTGTGCCT	3'

12-arm star:

strand 1	5'	AGGCACAGCTATAATAACGCAATCCTCTCCGGCCTCAAACTACTTTACCT	3'
strand 2	5'	AGGTAAAGTAGTTTGAGGCCGGAGACCGAATGGAGTCTGTTCTCGACGCT	3'
strand 3	5'	AGCGTCGAGAACAGACTCCATTCGGACAATTACGAACCAACTTAGGACCT	3'
strand 4	5'	AGGTCCTAAGTTGGTTCGTAATTGTGGTCATCGTGGCGTACCATATACCT	3'
strand 5	5'	AGGTATATGGTACGCCACGATGACCTCTTCGATCTACCCGATAGGCTCCT	3'
strand 6	5'	AGGAGCCTATCGGGTAGATCGAAGACGTACAGGTGTGACTTGAATTTGCT	3'
strand 7	5'	AGCAAATTCAAGTCACACCTGTACGAGTGTTAGAATACAACAAGCGACCT	3'
strand 8	5'	AGGTCGCTTGTTGTATTCTAACACTGCATCTCATACGGCAGTATCCGCCT	3'
strand 9	5'	AGGCGGATACTGCCGTATGAGATGCTGAGCACGGAACTGTCAACCTTGCT	3'
strand 10	5'	AGCAAGGTTGACAGTTCCGTGCTCACGTTCATTAAGATAAATCTGATCCT	3'
strand 11	5'	AGGATCAGATTTATCTTAATGAACGACTATGCCTGCTACATGCACTTCCT	3'
strand 12	5'	AGGAAGTGCATGTAGCAGGCATAGTGGATTGCGTTATTATAGCTGTGCCT	3'

Supplementary Section S2: Investigation of Shallow Events from 12-arm

For the 12-arm star nanostructure, a faster migrating streaking band is often present, indicating up to 45% of the portion could be misassembled depending on the production batch. This streaking band is less pronounced when a small mass of the 12-arm star is loaded into the gel (500 ng compared to 25 ng), due to the limitation in the resolution of the gel imaging device.

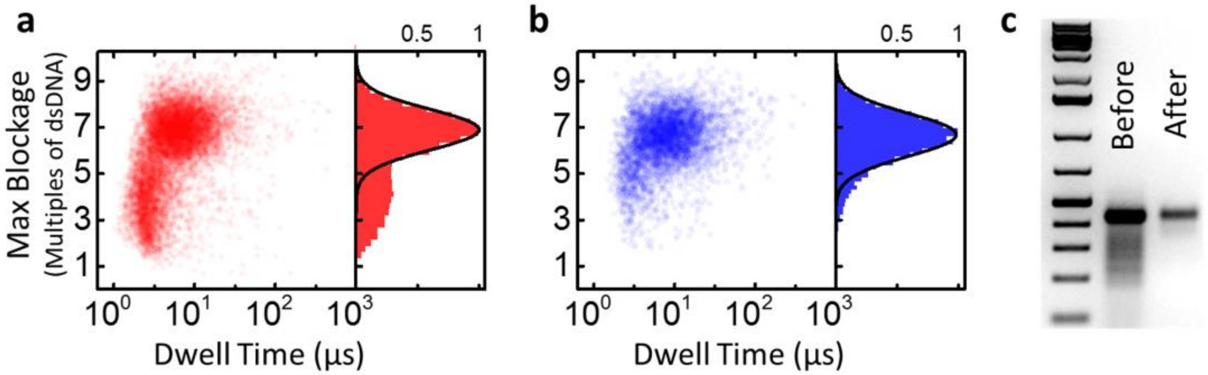

Supplementary Figure S1. Purification results of 12-arm. **(a)** Scatter plot of unpurified 12-arm star showing 29% shallow events. **(b)** Scatter plot of purified 12-arm star with 7% shallow events. Both experiments are performed in LiCl pH 8.0, using the same pore of 11.5 nm in diameter with an applied bias of 200 mV. **(c)** Gel electrophoresis results in 2% agarose gel in 1xTAE, from left to right: GeneRuler 1 kb Plus DNA Ladder (Thermo Scientific, SM1331), 12-arm star following assembly, and 12-arm star after purification. On the ladder lane of the gel image shows from bottom to top: 200, 300, 400, 500, 700, 1000, 1,500 bp, etc.

Misassembled products account for the major portion of the shallow events observed (Figure 4b). Supplementary Figure S1a shows the scatter plot of 12-arm star before purification showing 29% of such shallow events (extracted from the Gaussian fit of the histogram). The crude products can then be purified using a method described by Sun *et al.*[2], as commercial gel extraction kits have been observed to disassemble DNA origami structures. Briefly, the desired band is visualized using UV light and extracted from a 2% agarose gel. The excised band can be purified using the diffusion method as described by Alibakhshi *et al.*[3]. The gel image of the purified

12-arm shows that most of the streaking is removed in comparison to the unpurified 12-arm (Supplementary Figure S1c).

Supplementary Figure S1b shows the scatter plot of purified 12-arm star with only ~7% shallow events, indicating that the purification step significantly reduced the rate of shallow events. The remaining shallow events could be explained by a combination of factors such as the bandwidth of the recording device producing truncated events when the passage times are short and approaching the ~1 μs response time of our system, or the possibility of collisions of labels that do not fully translocate. However, the dramatic reduction in the shallow event rate after purification strongly suggests that these events are due to remaining misassembled products, as a faint streak can be still be seen on Figure S1c, either due to partial dissociation of nanostructures during or after the purification step or remaining misassembled products in the excised gel as due to the limitation of this manual band cutting step.

To further highlight the effect of the time resolution of our measurements system (nanopore device + sensing electronics) on the ability to detect these shallower events, we show translocation results from 4 additional pores ranging in size from 7.5 to 10.5 nm, each at two different voltages. The results shown in Supplementary Figure S2 demonstrate how some of the shallow events can be missed by our measurement system when the voltage is increased, and the passage times are faster than ~4 μs (before which events have not yet reached the full depth). In particular, data on the smaller 7.5 nm pore (Supplementary Figure S2d) show a better-resolved distribution of shallow events compared to data acquired on larger pores. On that pore, when the voltage is increased, the shallow events are compressed around ~4 μs, the minimum timescale for our measurement system to not attenuate the depth of events, and where many are missed, much like in the other data sets. On the other hand, the events from the fully formed 12-arm products continue to show a measurable reduction in the mean passage time when the voltage in increased, as in the other data sets and as is expected.

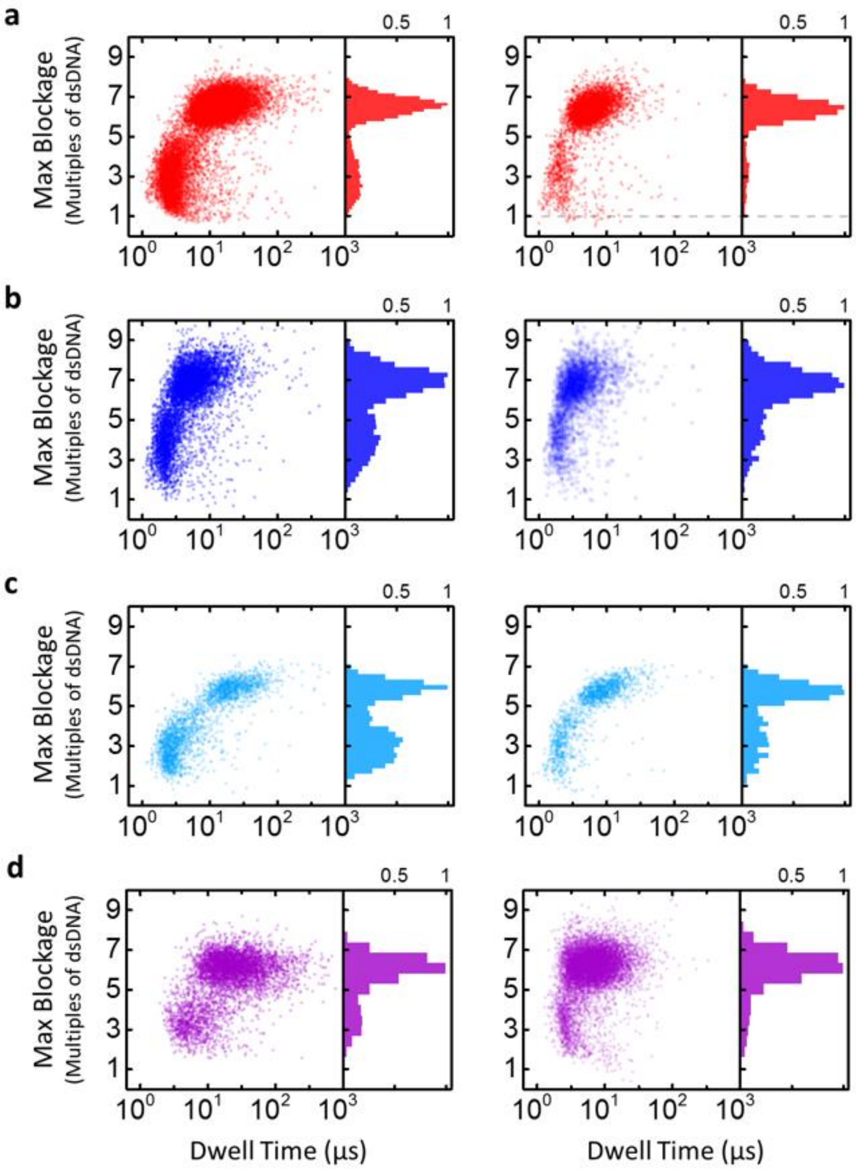

Supplementary Figure S2. Scatter plots of 12-arm star. **(a)** Scatter plot of maximum blockage *versus* dwell time using an 8.8 nm pore, with an applied bias of 200 mV (left) and 300 mV (right). **(b)** Scatter plot of maximum blockage *versus* dwell time using a 10.5 nm pore, with an applied bias of 200 mV (left) and 250 mV (right). **(c)** Scatter plot of maximum blockage *versus* dwell time using an 8.7 nm pore, with an applied bias of 200 mV (left) and 300 mV (right). **(d)** Scatter plot of maximum blockage *versus* dwell time using a 7.5 nm pore, with an applied bias of 100 mV (left) and 200 mV (right).

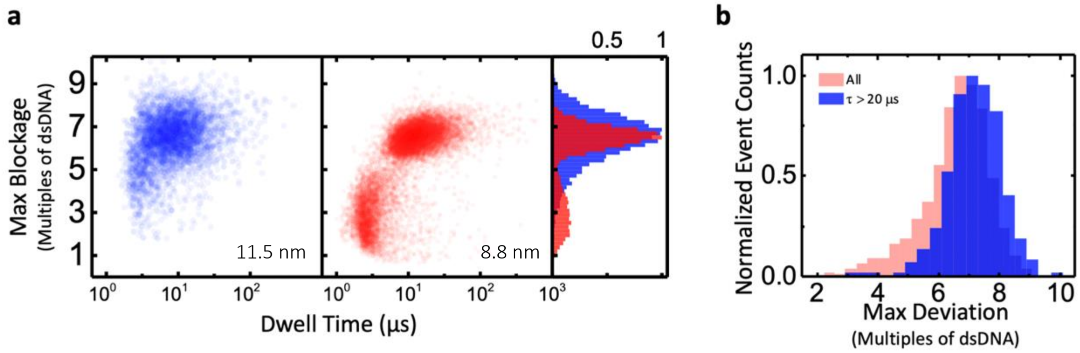

Supplementary Figure S3. Scatter plots and histograms of the 12-arm star. **(a)** Scatter plots of the 12-arm star using an 8.8 nm pore (red, n = 16,822) *versus* an 11.5 nm pore (blue, n = 5,005), with an applied bias of 200 mV in symmetric 3.6 M LiCl pH 8. **(b)** Distributions of the 12-arm star on the 11.5 nm pore, entire data set (pink, n = 5,005) *versus* subset of data with events longer than 20 μs (blue, n = 583).

The scatter plot and histogram of the 12-arm star using an 8.8 nm pore (red) versus an 11.5 nm pore are shown in Supplementary Figure S3a. Note that data using an 8.8 nm pore (red in Supplementary Figure S3a) was collected with the 12-arm star without any purification, the low-level shallow events can be eliminated by the purification technique described above. Despite this, the distributions of the fully formed 12-arm using both 8.8 nm and 11.5 nm pore have the same mean maximum blockage. The 12-arm star on a larger pore has a shorter mean dwell time (7 ± 2 μs in an 11.5 nm pore *versus* 12 ± 2 μs in an 8.8 nm pore), which results in a higher number of poorly fitted events because many events are short-lived (<10 μs), and therefore the distribution has larger spread.

For the 12-arm star data collected on an 11.5 nm data, if we plot only the subset of events with passage times longer than 20 μs, the spread of the distribution becomes smaller in comparison to the whole data set (Supplementary Figure S3b). This supports the argument that the spread in the distribution below $N/2$, 6 multiples of dsDNA in this case, is a result of poor fits of the short-lived events, since almost no events lasting longer than 20 μs exhibit a maximum deviation below 6x dsDNA. Here the maximum deviation is the single data point furthest away from the local open pore current in an event. The maximum deviation metric thus measures the deepest sublevel of any event that is detected by the hardware, plus contribution of noise.

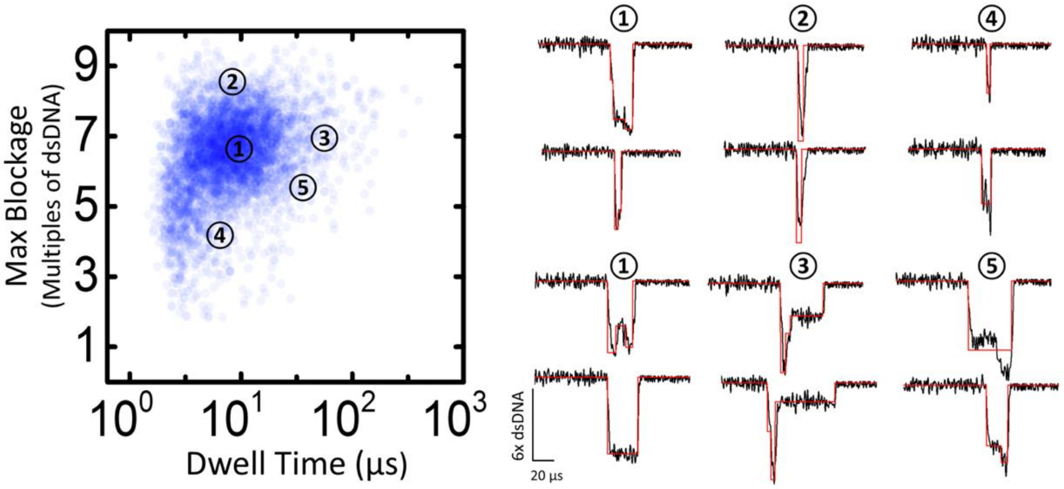

Supplementary Figure S4. Scatter plot of the 12-arm star using an 11.5 nm pore with an applied bias of 200 mV in symmetric 3.6 M LiCl pH 8, and the current traces corresponding to different regions, with fits in red.

Supplementary Figure S4 shows the scatter plot of the 12-arm star using an 11.5 nm pore and the current traces corresponding to each region of the scatter plot. Current traces from region 1 (events around the mean) and 3 (long-lived events) show events that are correctly fitted. Currents traces from region 4 (short-lived events below the minimal anticipated max blockage) show examples of events whose deepest levels are not fitted correctly, or the deepest levels are not resolved at all. Current traces from region 5 (long-lived events at the minimal anticipated max blockage) show examples of misfits of longer events, although the whole events are relatively long, the deepest levels are still missed by our analysis algorithm in some cases. Current traces from region 2 (events with deep blockages) show an example of a correctly fitted event and an event which is over-estimated due to fitting. In conclusion, the spread of the distribution of the star-shaped molecules are partially caused by a combination of misassembled products (very short shallow events), and the quality of the fits (under-estimation and over-estimation) of shorter events and the limitation of the resolution of our recording device.

Supplementary Section S3: Additional 4-arm and 6-arm Results

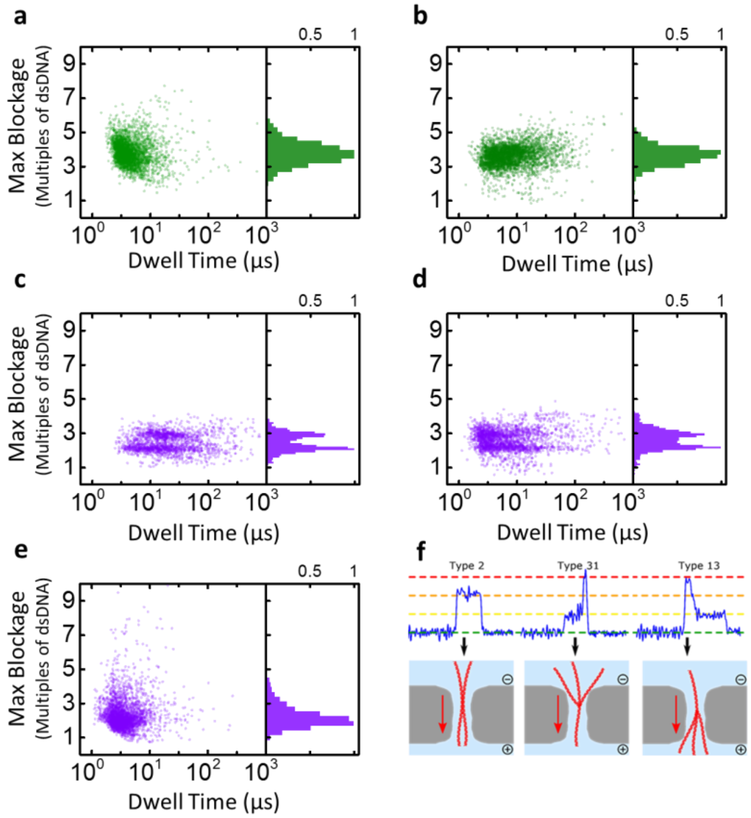

Supplementary Figure S5. (a) Scatter plot for 6-arm star DNA of normalized maximum blockage *versus* dwell time in a 9.7 nm pore with an applied bias of 200 mV. **(b)** Scatter plot for 6-arm star DNA of normalized maximum blockage versus dwell time in a 7.4 nm pore with an applied bias of 200 mV. **(c)** Scatter plot for 4-arm star DNA of normalized maximum blockage *versus* dwell time using a 5.6 nm pore with an applied bias of 200 mV. **(d)** Scatter plot for 4-arm star DNA of normalized maximum blockage *versus* dwell time using a 5.6 nm pore with an applied bias of 400 mV. **(e)** Scatter plot for 4-arm star DNA of normalized maximum blockage *versus* dwell time using a 9 nm pore with an applied bias of 200 mV. **(f)** Example events from **(c-d)**. All experiments are performed in 3.6 M LiCl pH8 and analyzed at 500 kHz.

The gel electrophoresis results for the 6-arm dsDNA star label are shown in Figure 1b in the main manuscript, indicating correct assembly for the majority of the product. The 6-arm star labels are then characterized by solid-state nanopores, immersed in 3.6 M LiCl pH 8.0 with an applied bias of 200 mV. Supplementary Figure S5a-b show the translocation characteristics of the 6-arm dsDNA star label in two different nanopores. The blockage depth histograms are fitted with a single peak Gaussian to extract the mean maximum blockage as described previously. The scatter plot from the 9.7 nm nanopore (Supplementary Figure S5a) shows a mean maximum blockage of

3.7 ± 0.6 multiples of dsDNA, and the scatter plot from the 7.4 nm nanopore (Supplementary Figure S5b) shows a mean maximum blockage of 3.6 ± 0.5 multiples of dsDNA. The mean maximum blockage of the 6-arm star label is more than 3x deeper than the expected blockage of dsDNA, suggesting that it is translocating most likely in a 3-arm/3-arm orientation and 4-arm/2-arm orientation, though we cannot resolve these two possibilities in the distribution, as discussed in the main text.

In contrast, the 4-arm label translocating a small 5.6 nm pore (compared to a 9.0 nm in Figure 2 of the main manuscript) now shows two clear distinct populations in the maximum blockade distribution at an applied bias of 200 mV (Supplementary Figure S5c), the deeper events have a mean maximum blockage of 2.9 ± 0.2 multiples of dsDNA indicating that the label is translocating in either a 3-arm/1-arm or the 1-arm/3-arm orientation, and the lower events have a mean maximum blockage of 2.3 ± 0.2 multiples of dsDNA indicating a 2-arm/2-arm orientation during translocation. Increasing the applied bias to 400 mV (Supplementary Figure S5d), the 3-arm/1-arm population shows a mean maximum blockage of 2.9 ± 0.3 multiples of dsDNA and the 2-arm/2-arm population shows a mean maximum blockage of 2.1 ± 0.2 multiples of dsDNA. The observation of these discrete sublevels for the 4-arm label on a 5.6 nm pore, which are attributed to distinct orientations during translocation, is made possible by the small size of the pore slowing the passage of the nanostructures, restricting their conformation and forcing specific orientations.

Supplementary Section S4: Additional 2-plex Results

In addition to the multiplexing results shown in the main manuscript in Figure 4, additional 2-plex experiments were performed under similar conditions as shown in Supplementary Figure S6, and without purifying the labels. The 8-arm star label shows a mean maximum blockage of 3.9 ± 0.7 multiples of dsDNA and 1.5 % of shallow events outside the Gaussian fit. The 12-arm star label shows a mean maximum blockage of 6.8 ± 0.7 multiples of dsDNA and 22.8 % of shallow events outside the Gaussian fit. These results show that we can distinguish with a confidence interval of 95 % or better 4-arm from 8-arm, and 8-arm from 12-arm. Purifying the DNA nanostructures to remove partially assembled structures would further improve the separation between the peaks (see section S2).

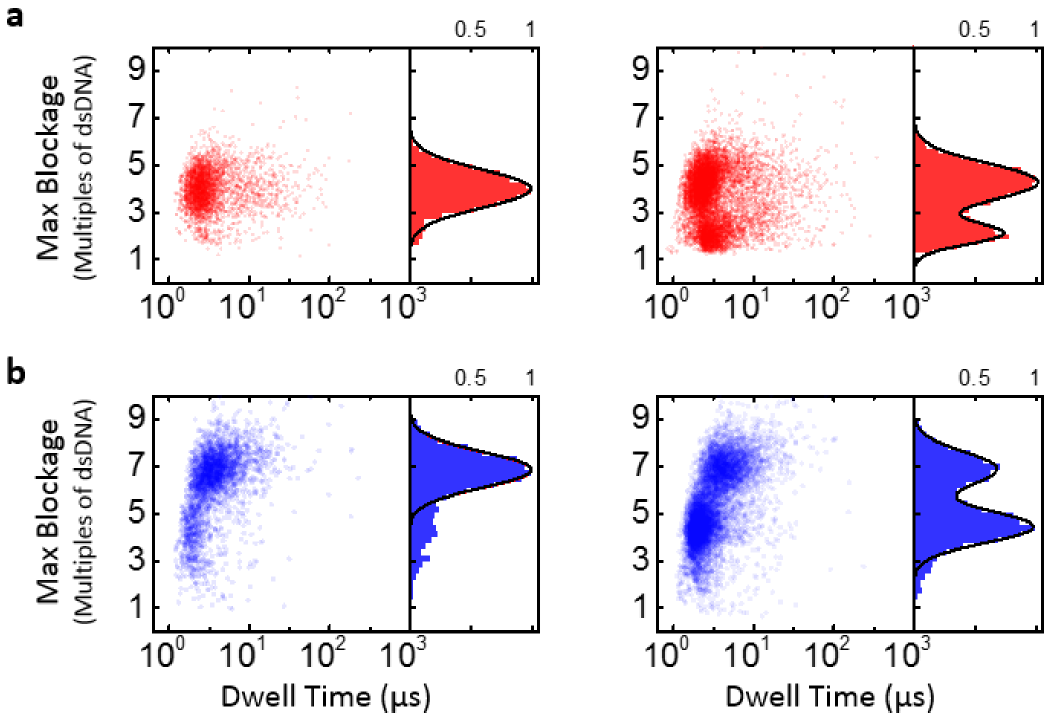

Supplementary Figure S6. Scatter plots of 2-plexing. **(a)** Scatter plot of normalized maximum blockage *versus* dwell time for the unpurified mixture of 4-arm and 8-arm stars using a 13.4 nm pore at 200 mV in comparison with the scatter plot of 8-arm alone on the left. **(b)** Scatter plot of normalized maximum blockage *versus* dwell time for the unpurified mixture of 8-arm and 12-arm stars using a 10.6 nm pore at 250 mV in comparison with the scatter plot of unpurified 12-arm alone on the left. Distributions of corresponding maximum blockage are attached to each scatter plots. Experiments are performed in 3.6 M LiCl, pH 8.0, and analyzed at 500 kHz.

Supplementary Section S5: Additional Salt Asymmetry Results

Supplementary Figure S7a shows the capture rate improvement as a function of salt concentration asymmetry for 8-arm and 12-arm dsDNA star labels for 5 different solid-state nanopores. In addition to the 200-fold increase in capture rate, an increase of up to 20-fold in the average dwell time is observed (Supplementary Figure S7b) when going from C_{trans}/C_{cis} = 3.6 M/3.6 M = 1 to C_{trans}/C_{cis} = 3.6 M/ 0.18 M = 20. Interestingly, a salt gradient in either directions ($C_{trans}/C_{cis} < 1$ and $C_{trans}/C_{cis} > 1$) appears to significantly increase the average dwell time, i.e. the shortest average dwell time is observed in symmetric salt. This is consistent with the salt asymmetry results for linear dsDNA by Wanunu *et al.*[3], where a 3.5x increase in average dwell time for 2,000 bp dsDNA is achieved.

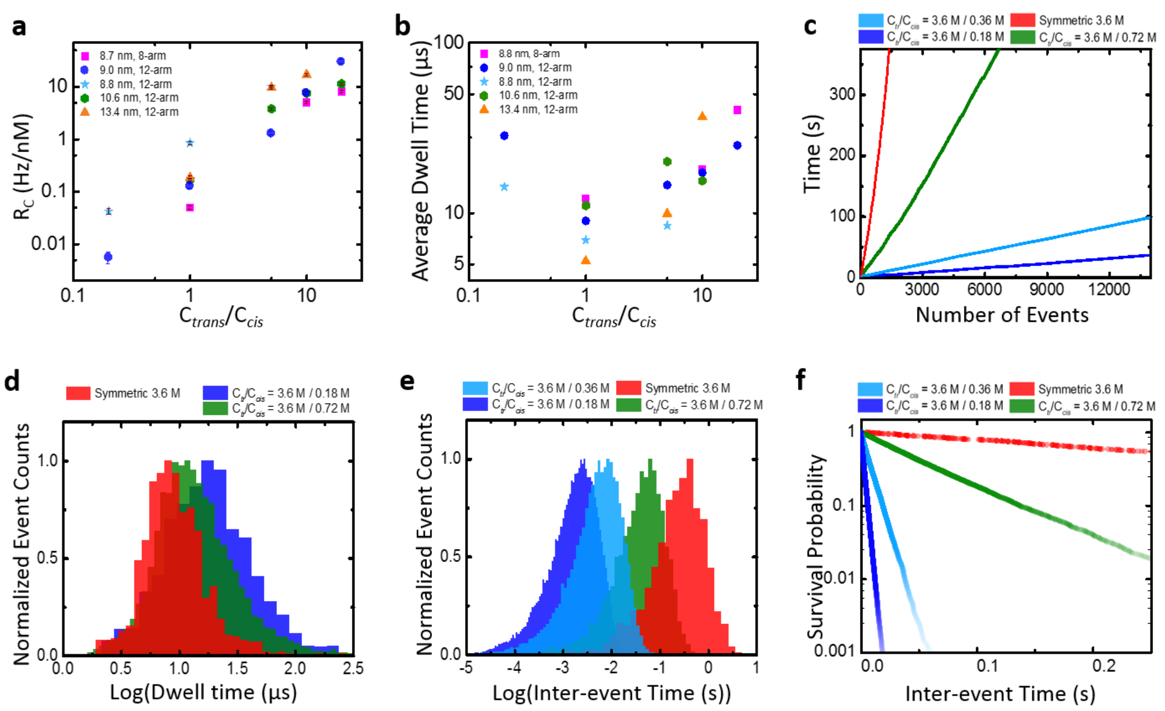

Supplementary Figure S7. Improvement of capture rate and average dwell time for 8-arm and 12-arm star labels. **(a)** Capture rate *versus* salt gradient (C_{trans}/C_{cis}) on a log-log scale. **(b)** Average dwell time *versus* salt gradient (C_{trans}/C_{cis}) for the 12-arm star on a log-log scale. Experiments are performed with an applied bias of 200 mV in LiCl with the following ratio and absolute values of concentrations: C_{trans}/C_{cis} = 0.72 M/ 3.6 M = 0.2, C_{trans}/C_{cis} = 3.6 M/ 3.6 M = 1, C_{trans}/C_{cis} = 3.6 M/ 0.72 M = 5, C_{trans}/C_{cis} = 3.6 M/ 0.36 M = 10, C_{trans}/C_{cis} = 3.6 M/ 0.18 M = 20. **(c)** Time *versus* number of events for the 12-arm star for various asymmetric LiCl salt conditions. **(d)** Distribution of translocation time for the 12-arm star for symmetric 3.6 M/ 3.6 M LiCl compared to C_{trans}/C_{cis} = 5, 10 and 20. **(e)** Distribution of inter-event time for C_{trans}/C_{cis} = 10 and 20 compared to symmetric 3.6 M/3.6 M LiCl. **(f)** Survival probability *versus* inter-event time for symmetric and asymmetric LiCl salt. All experiments in (c,d,e,f) are performed using a 9 nm pore with an applied bias of 200 mV.

Supplementary Figure S7 (c), (d), (e) and (f) show the distribution of inter-event times and the cumulative number of events as a function of time to demonstrate that arrival time of molecules at the pore follows the expected (time-invariant) Poisson process. This suggests that the events detected are fully translocating so that no molecules are counted multiple times.

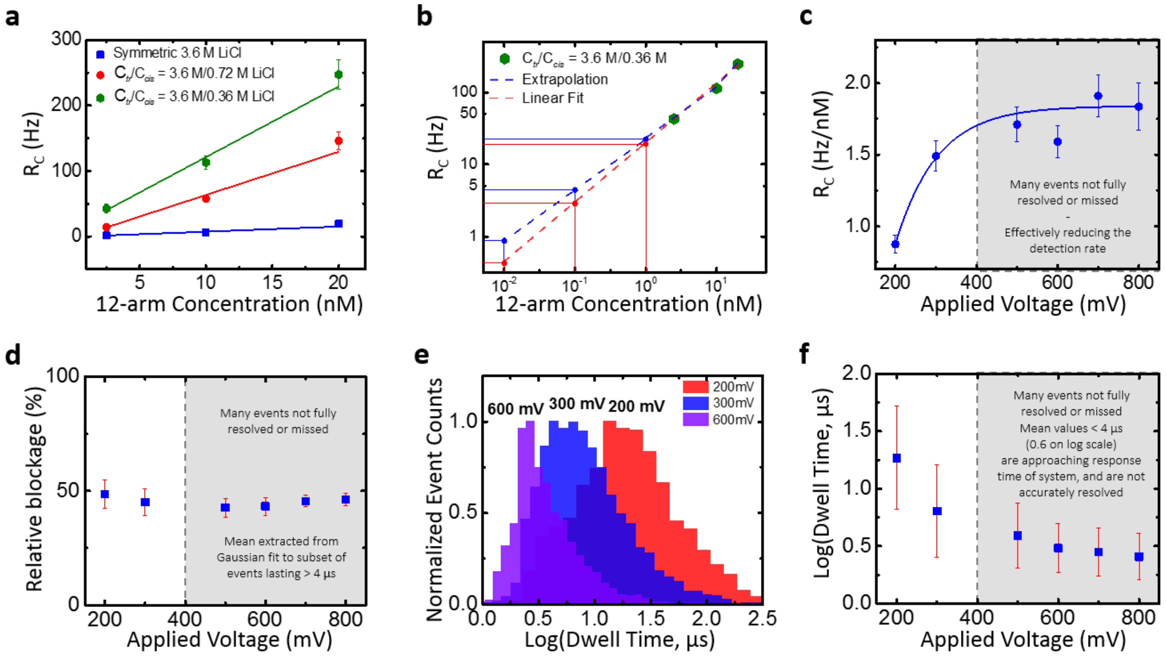

Supplementary Figure S8. Voltage dependence of the 12-arm star in asymmetric LiCl salt conditions using a 10.3 ±0.3 nm pore. **(a)** Capture rate of the 12-arm star as a function of its molar concentration for symmetric and asymmetric LiCl, at 200 mV. **(b)** Extrapolation to pico-molar range (10 pM and 100 pM) for asymmetric C_{trans}/C_{cis} = 0.36 M/3.6 M LiCl, at 200 mV. **(c, d and f)** Capture rate, relative blockage and dwell time of the 12-arm star *versus* applied voltage in symmetric 0.72 M/0.72 M LiCl. **(e)** Distribution of dwell time for 200 mV, 300 mV and 600 mV in symmetric 0.72 M/0.72 M LiCl.

Supplementary Figure S8a shows capture rate of the 12-arm star as a function of its concentration (from 2.5 nM to 20 nM) for symmetric 3.6 M LiCl, C_{trans}/C_{cis} = 3.6 M/0.72 M and C_{trans}/C_{cis} = 3.6 M/0.36 M. The capture rate for the 12-arm star at 10 pM can be extrapolated for the asymmetric C_{trans}/C_{cis} = 3.6 M/0.36 M case, we estimate a capture rate of 0.9 Hz and 0.4 Hz from interpolation and linear fit, respectively (Figure S8b). This shows the potential of picomolar concentration measurements while overcoming the challenges of analyzing short-lived translocation events.

Supplementary Figure S8d shows that the relative blockage level (extracted from Gaussian fit) of the 12-arm star in symmetric 0.72 M LiCl does not appear to be affected by voltage (from 200 mV to 800 mV) and stays close to 50%, indicating that the 12-arm events are indeed translocations rather than collisions with the pore. This is supported by the fact that the average dwell time decreases with increasing voltage as shown in Supplementary Figure S8e-f.

As the applied voltage is increased over 500 mV, the 12-arm stars translocation events become too fast and many events are missed, and it becomes more difficult fit them correctly. This is reflected on Supplementary Figure S8f where the decrease in dwell time is attenuated and flattens out. Furthermore, the capture rate stops increasing once the applied voltage passes the 500 mV as shown in Supplementary Figure S8c, indicating by events are more events are missed with increasing voltage above 500 mV.

Supplementary Information S6: Pore Statistics

The effective pore length were calibrated by using long linear dsDNA as a molecular ruler [4], while in 3.6M LiCl pH8. The effective pore size is calculated based on the pore conductance and the effective pore length.

Pore ID	Applied Voltage (mV)	Mean Baseline Level (nS)	Effective Pore Length (nm)	Effective Pore Size (nm)
P1	200	25.2 ± 0.4	5.5 ± 0.3	4.2 ± 0.1
P2	400	12.8 ± 0.2	10.0 ± 0.3	3.6 ± 0.1
P3	200	59.6 ± 0.4	10.9 ± 0.3	9.2 ± 0.1
P4	200	34.3 ± 0.2	11.4 ± 0.4	6.7 ± 0.1
P5	200	21.6 ± 0.2	10.8 ± 0.2	5.0 ± 0.1
P6	200	44.9 ± 0.2	12.3 ± 0.3	8.1 ± 0.1
P7	200	41.5 ± 0.2	10.3 ± 0.2	7.2 ± 0.1
P8	400	15.6 ± 0.2	10.5 ± 0.2	4.1 ± 0.1
P9	400	21.4 ± 0.1	13.9 ± 0.2	5.5 ± 0.1
P10	400	36.0 ± 0.1	13.4 ± 1.0	7.4 ± 0.1
P11	200	26.3 ± 0.2	10.9 ± 0.7	5.6 ± 0.2
P12	200	31.2 ± 0.2	8.9 ± 0.1	5.7 ± 0.1
P13	200	40.0 ± 0.2	9.6 ± 0.1	7.2 ± 0.1
P14	400	37.0 ± 0.1	9.1 ± 0.2	6.7 ± 0.1
P15	200	54.3 ± 0.3	12.8 ± 0.3	9.7 ± 0.1
P16	200	33.8 ± 0.3	11.9 ± 0.2	7.1 ± 0.1
P17	200	33.9 ± 0.2	12.2 ± 0.3	7.1 ± 0.1
P18	200	37.5 ± 0.2	12.6 ± 0.4	7.4 ± 0.1
P19	200	45.9 ± 0.4	14 ± 0.4	8.8 ± 0.1
P20	200	74.7 ± 0.5	13.3 ± 0.7	11.6 ± 0.2
P21	200	55.0 ± 0.6	12.9 ± 0.6	9.5 ± 0.2
P22	200	41.6 ± 0.4	10.7 ± 0.3	7.4 ± 0.1
P23	200	47.6 ± 0.5	13.3 ± 0.4	8.8 ± 0.1
P24	200	86.9 ± 1.4	13.3	13.4
P25	200	75.6 ± 1.6	12.5 ± 0.4	11.4 ± 0.3
P26	200	61.8 ± 0.9	12.9 ± 0.3	10.6 ± 0.2
P27	200	63.5 ± 1.5	12.8 ± 0.4	10.3 ± 0.3
P28	200	52.3 ± 1.1	12.5 ± 0.3	9.0 ± 0.2
P29	200	75.4 ± 1.3	13.8 ± 0.4	12.5 ± 0.3
P30	200	82.2 ± 1.1	12.1 ± 0.3	11.5 ± 0.3

References

(1) Wang, X.; Seeman, N. C. Assembly and Characterization of 8-Arm and 12-Arm DNA Branched Junctions. *J. Am. Chem. Soc.* **2007**, *129* (26), 8169–8176. https://doi.org/10.1021/JA0693441.

(2) Sun, Y.; Sriramajayam, K.; Luo, D.; Liao, D. J. A Quick, Cost-Free Method of Purification of DNA Fragments from Agarose Gel. *J Cancer* **2012**, *3* (22*)*, 93–95. https://doi.org/10.7150/jca.4163.

(3) Alibakhshi, M. A.; Halman, J. R.; Wilson, J.; Aksimentiev, A.; Afonin, K. A.; Wanunu, M. Picomolar Fingerprinting of Nucleic Acid Nanoparticles Using Solid-State Nanopores. *ACS Nano* **2017**, *11* (10), 9701–9710. https://doi.org/10.1021/acsnano.7b04923.

(4) Karau, P.; Tabard-Cossa, V. Capture and Translocation Characteristics of Short Branched DNA Labels in Solid-State Nanopores. *ACS Sensors* **2018**, *3* (7), 1308–1315. https://doi.org/10.1021/acssensors.8b00165.